Cell Reports

Mechanisms governing poly(A)-tail-length specificity of the human PAN2-PAN3 deadenylase complex

Graphical abstract

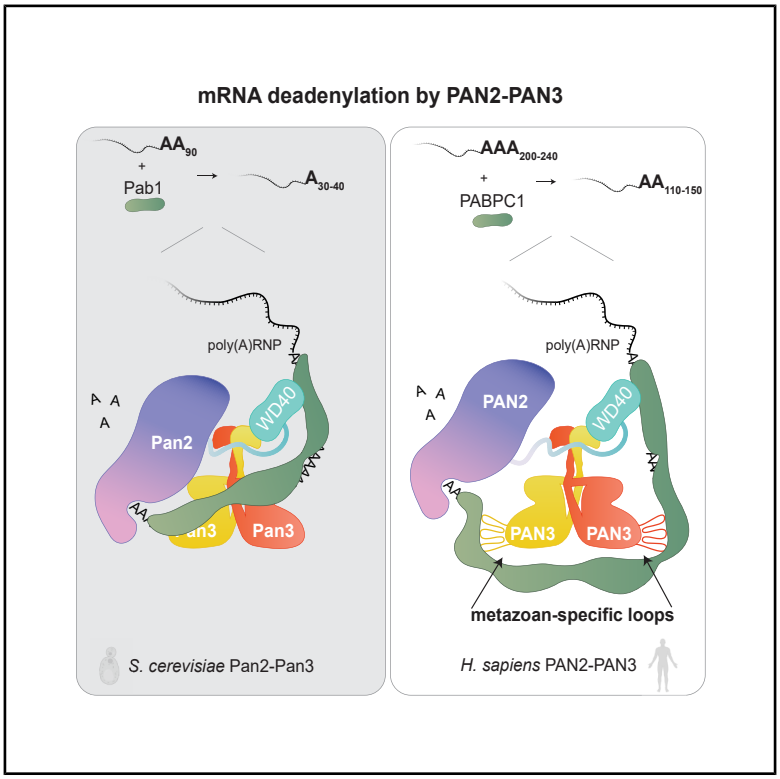

Highlights

- Methodology to synthesize and purify defined poly(A) RNAs up to 240 nt
- *In vitro* assays mirror the preference of human PAN2-PAN3 for long poly(A) tails
- Human PAN2-PAN3 uses distinct binding sites to accommodate long-poly(A)-tail RNPs
- Metazoan-specific loop regions of human PAN3 define the poly(A) tail binding path

Authors

Jana C. Albrecht, Timo Reitinger, Jérôme Basquin, Steffen Schüssler, Margot Riggi, Ingmar B. Schäfer, Elena Conti

Correspondence

ingmar.schaefer@tu-dresden.de (I.B.S.), conti@biochem.mpg.de (E.C.)

In brief

PAN2-PAN3 deadenylases are conserved but act on mRNA poly(A) tails of different lengths in yeast and human. Albrecht et al. show how metazoan-specific loops in PAN3 create distinct binding sites for poly(A)-PABPC1 ribonucleoproteins, favoring longer poly(A) tails than in yeast and rationalizing these substrate preferences.

Albrecht et al., 2025, Cell Reports *44*, 116609
December 23, 2025 © 2025 The Authors. Published by Elsevier Inc.
https://doi.org/10.1016/j.celrep.2025.116609

CellPress

Cell Reports

CellPress
OPEN ACCESS

Report

Mechanisms governing poly(A)-tail-length specificity of the human PAN2-PAN3 deadenylase complex

Jana C. Albrecht,[1,5] Timo Reitinger,[1,5] Jérôme Basquin,[1] Steffen Schüssler,[1] Margot Riggi,[1] Ingmar B. Schäfer,[2,3,4,*] and Elena Conti[1,6,*]

[1]Department of Structural Cell Biology, Max Planck Institute of Biochemistry, Am Klopferspitz 18, Martinsried, 82152 Munich, Germany
[2]Center of Membrane Biochemistry and Lipid Research, University Hospital and Faculty of Medicine Carl Gustav Carus, Technical University Dresden, Dresden, Germany
[3]Paul Langerhans Institute Dresden (PLID) of the Helmholtz Center Munich, University Hospital and Faculty of Medicine Carl Gustav Carus, Technical University Dresden, Dresden, Germany
[4]German Center for Diabetes Research (DZD), Neuherberg, Germany
[5]These authors contributed equally
[6]Lead contact
*Correspondence: ingmar.schaefer@tu-dresden.de (I.B.S.), conti@biochem.mpg.de (E.C.)
https://doi.org/10.1016/j.celrep.2025.116609

SUMMARY

The lifespan of most eukaryotic mRNAs is modulated by the gradual shortening of the poly(A) tail and removal of the associated poly(A)-binding protein. The human PAN2-PAN3 complex catalyzes initial deadenylation by shortening long poly(A) tails associated with PABPC1. Both PAN2-PAN3 and PABPC1 are evolutionarily conserved from fungi to humans. How the human complex has adapted to recognize and act on longer poly(A) tails characteristic of mammalian mRNAs remains unclear. Here, we report a method to obtain homo-polymeric poly(A) RNAs up to 240 nt, mimicking the synthesis length of poly(A) tails in mammals. We recapitulate human deadenylation properties *in vitro*, with PAN2-PAN3 showing greater activity on long poly(A)-PABPC1 ribonucleoprotein substrates. Single-particle cryo-electron microscopy (cryo-EM) analyses of PAN2-PAN3 bound to poly(A)-PABPC1 ribonucleoproteins uncover a longer substrate-binding path in the case of the human deadenylase compared to fungi. Altogether, these data provide a rationale for the co-evolution of deadenylase properties and poly(A) tail lengths.

INTRODUCTION

The poly(A) tail is a major regulator of the stability of eukaryotic mRNAs and their ability to be translated into protein.[1,2] This crucial feature of mature mRNAs is added to the 3′ end upon transcription termination, with an average native length of ~200–240 nt in human cells and ~90 nt in budding yeast.[3] Generally, poly(A) tails do not exist as bare nucleic acid stretches but are instead associated with poly(A)-binding proteins.[3] In the cytoplasm, the poly(A)-binding protein (PABPC1 in humans and Pab1 in *S. cerevisiae*) is expected to coat the poly(A) tails in their entirety.[4] The resulting poly(A) tail ribonucleoprotein (RNP) protects the body of the mRNA from nonspecific degradation by exoribonucleases. Simultaneously, however, the poly(A) RNP is also a binding platform for deadenylase complexes (PAN2-PAN3 and CCR4-NOT) that specifically trim the 3′ end of the transcript in a stepwise manner, a process that is often a hotspot of regulation in gene expression pathways.[1]

A current working model, based on *in vivo* data, proposes a coordinated deadenylation process, whereby the PAN2-PAN3 complex preferentially erodes long-poly(A)-tail RNPs, whereas the CCR4-NOT complex degrades shorter-poly(A)-tail RNPs to initiate the decay of the transcript.[5,6] The transition between the two deadenylases has been estimated to occur between 110 and 150 nt in human cells[5,7] and at about 30–40 nt in budding yeast[8–10]—coinciding roughly with the estimated steady-state lengths in the two organisms.[11,12] Our previous biochemical and structural studies on *S. cerevisiae* Pan2-Pan3 in complex with a 90A RNA bound to three Pab1 molecules revealed the molecular mechanisms underlying Pan2-Pan3 poly(A) tail substrate preference in yeast.[13] Given the strong evolutionary conservation at the protein level between the yeast and human deadenylases, it is thus perplexing how human PAN2-PAN3 exhibits such different substrate preference *in vivo*. Here, we set out to understand the molecular basis of human PAN2-PAN3 poly(A) tail shortening, a process that is interesting both from an evolutionary perspective and for its significance at the organismal level and in the context of disease. Indeed, missense and nonsense mutations in human *PAN2* are connected to intellectual and developmental deficits in humans.[14,15] We report that structural differences in surface-exposed loop regions of the PAN3 subunit, compared to the yeast protein, allow it to recognize longer poly(A) RNP substrates.

This is an open access article under the CC BY license (http://creativecommons.org/licenses/by/4.0/).

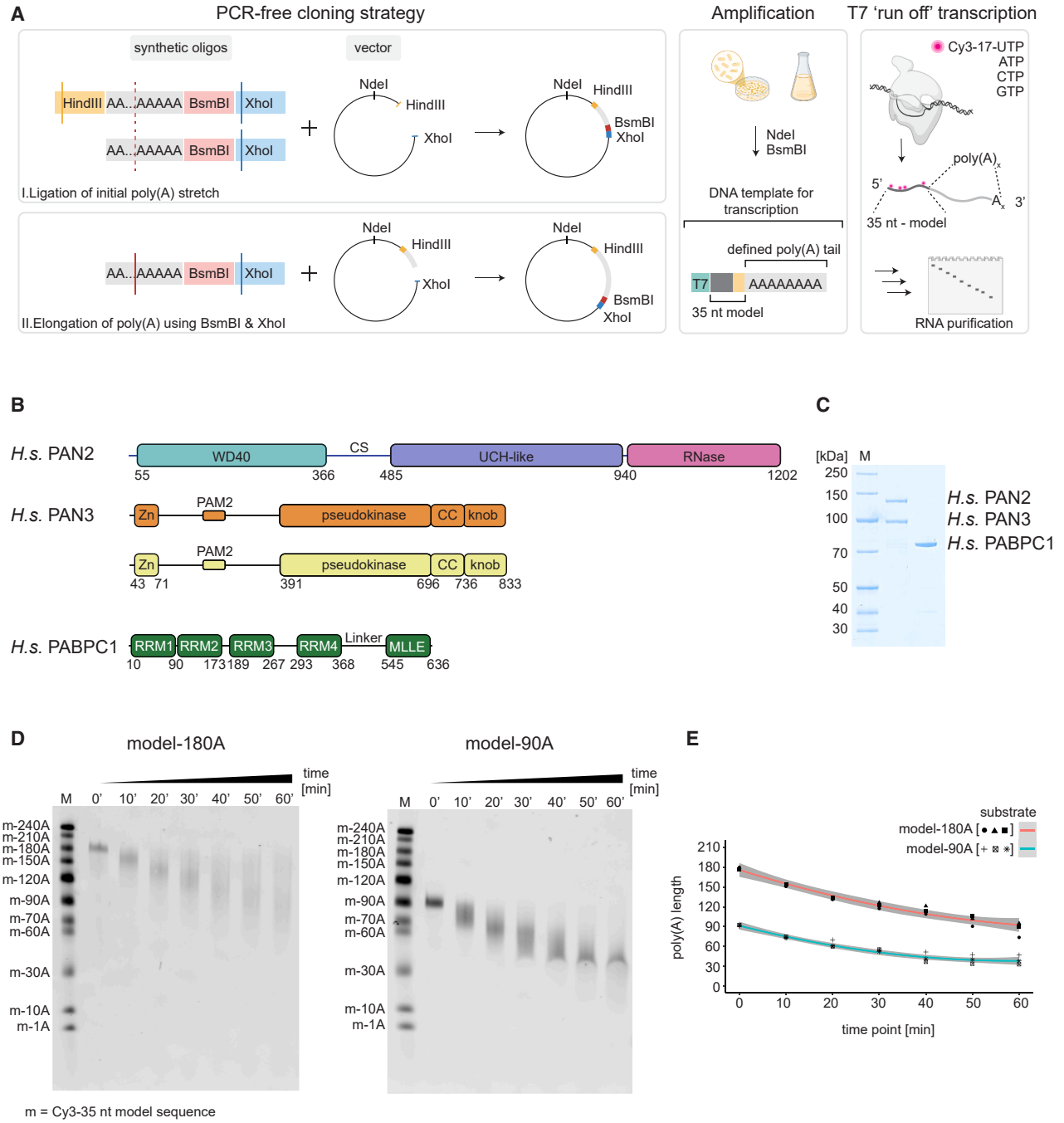

Figure 1. *H. sapiens* PAN2-PAN3 deadenylation activity on long and short poly(A) RNPs

(A) Scheme of cloning strategy for DNA templates and amplification and T7 RNA-polymerase-mediated *in vitro* transcription of long poly(A) tails. Cleavage sites for restriction endonucleases are indicated by colors and labeled accordingly. The PCR-free cloning strategy (similar to that used in Scior et al.[16]) in the first step involved ligation of two antiparallel annealed, synthetic oligonucleotides into the HindIII and XhoI digested pcDNA3.1 vector. For length-controlled elongation, XhoI and the type IIS endonuclease BsmBI were used. Plasmid amplification was carried out in *E. coli* cells. After plasmid preparation, the DNA was digested with NdeI and BsmBI. Resulting transcription templates were subjected to *in vitro* T7 run-off transcription, which incorporated Cy3-17-UTP in the ~35 nt at the 5′ end preceding the poly(A) tail of the model RNAs. The scheme was partially created with BioRender.com.

(B) Domain organization of human PAN2-PAN3 and PABPC1. Folded domains are shown as rectangles and sequences with low complexity as bars. The numbers refer to the domain boundaries. We used the published "short" splice variant of *H. sapiens* PAN3.[17] UCH, ubiquitin C-terminal hydrolase; Zn, zinc finger; CC, coiled-coil domain; RRM, RNA-recognition motif; MLLE, Mademoiselle domain.

(C) Coomassie-stained 4%–12% SDS-PAGE of isolated recombinant human PAN2-PAN3 and PABPC1. M indicates the molecular marker.

(legend continued on next page)

RESULTS

In vitro reconstitution of human PAN2-PAN3 deadenylase activity

We previously showed that a catalytically inactive human PAN2-PAN3 complex could interact with a 70A RNA bound to more than two PABPC1 protomers by size-exclusion chromatography experiments with recombinant proteins.[13] In contrast to yeast, however, a poly(A) tail of this length would be a suboptimal substrate for PAN2-PAN3 in human cells.[5] To establish a biochemical *in vitro* system that would mirror the *in vivo* properties of the human deadenylases, we first devised biochemical protocols to synthesize and purify longer poly(A) RNA substrates with defined lengths (Figures 1A and S1A–S1D). In a first step, a previously published PCR-free cloning strategy for repetitive DNA sequences was adapted to generate suitable DNA templates for *in vitro* transcription reactions.[16] We used successive ligation rounds to concatomerize annealed poly(A)/(T) oligos into vectors linearized with restriction enzymes, using a type II endonuclease that cleaves at the very 3′ end of the poly(A) stretches (Figure 1A). A crucial aspect to reach poly(A) lengths over 120A in these DNA templates was the identification of suitable DNA amplification conditions in *E. coli* that limit recombination events in the homo-typical adenosine stretches of the plasmids (see STAR Methods). The resulting plasmid series carrying poly(A) stretches of defined lengths was then digested with restriction endonucleases and used as templates in *in vitro* run-off transcriptions. Using this strategy, we generated a series of RNAs comprising a 35-nt sequence followed at the 3′ end by varying lengths of oligoA, ranging from 240 to 1 nt (named accordingly, i.e., model-240A or model-1A, respectively) (Figures S1C and S1D). To monitor degradation in deadenylation assays, the model substrates were fluorescently labeled with Cy3-UTP (cyanine 3-uridine-5′-triphosphate) during the *in vitro* transcription reaction (Figure 1A; with the exception of model-1A and model-10A, which were commercially synthesized). Recombinant PABPC1 and PAN2-PAN3 were purified similarly to before[13] except that we used the shorter isoform of PAN3, as it has been reported to interact more strongly with the poly(A)-binding protein (PAN3; Figures 1B and 1C).[17] To evaluate the deadenylation properties of PAN2-PAN3 *in vitro*, we compared two substrates that were respectively above and below the estimated transition region for substrate preference from *in vivo* data.[5,7] The model-180A and -90A RNPs were created with the corresponding RNAs in the presence of 1.5 molar excess of PABPC1. Upon incubation with PAN2-PAN3, all poly(A) RNPs were progressively degraded in a stepwise fashion at intervals corresponding to the expected PABPC1 footprint, about 27 nt per protomer (Figure 1D).[18] However, deadenylation proceeded approximately two times as fast on the longer transcripts (Figure 1E). We concluded that the *in vivo* deadenylation properties of human PAN2-PAN3 can be recapitulated biochemically *in vitro*.

Overall structure of human PAN2-PAN3

The domain organizations of human PAN2 and PAN3 (Figure 1B) are globally very similar to those of their orthologs from fungal species that have been characterized at the structural level.[13,19–23] We derived a human PAN2-PAN3 3D model by interpreting a single-particle cryo-electron microscopy (cryo-EM) reconstruction of the full-length complex with a rigid-body fitting of atomic models predicted using AlphaFold3 (Figures 2A, S2, and S3; Table S1). The structure of human PAN2-PAN3 recapitulated many of the conserved structural elements of orthologous complexes from fungi.[13,19–23] Briefly, PAN2-PAN3 has a 1:2 stoichiometry. While the N-terminal portion of PAN3 is intrinsically disordered, the C-terminal portion encompassing the pseudokinase, the coiled-coil (CC), and the so-called "knob" domains (Figure 1B) forms an intertwined homodimer through the intersection of the CC helices (Figure 2A). The two pseudokinase domains interact at one end of the CC (referred to as the bottom side of the homodimer), while the two knob domains interact at the other end (referred to as the top side). PAN2 binds at the top of the PAN3 homodimer, using the N-terminal WD40 domain and the "connecting segment" (CS) to interact with the composite surface formed by the two PAN3 knob domains (Figure 2A). In the PAN2 domain organization, the CS links to the enzymatic UCH-RNase module of the deadenylase, which contains an RNase domain of the DEDD family and a UCH-like domain with the fold of an inactive ubiquitin hydrolase (Figure 1B). In discussing the structure, we refer to the "proximal" and "distal" PAN3 pseudokinase domains to denote those located near the PAN2 WD40 domain and the UCH-RNase module, respectively. Compared to the *S. cerevisiae* core complex, human PAN2-PAN3, however, also showed notable differences. First, the UCH-RNase module of human PAN2 is more flexible and does not interact with the pseudokinase core of the human PAN3 homodimer. Second, human PAN3 has extended loop regions expected to protrude from the pseudokinase domain according to AlphaFold predictions, although we did not observe corresponding ordered density in the EM reconstruction of apo PAN2-PAN3 (Figure 2).

Structure of poly(A) RNP-bound human PAN2-PAN3

To capture the structure of human PAN2-PAN3 in complex with a long poly(A) RNP, we engineered the model-180A substrate to contain an inhibitory 3' end GGGAA sequence (model-180A$_i$) that is prone to stalling within the active site of the RNase,[19] incubated it with excess levels of PABPC1, and subjected it to cryo-EM analysis (Figures 2B and S2). We used a similar approach to visualize PAN2-PAN3 in complex with a 90A$_i$ RNP. This poly(A)

(D) Deadenylation time course of model-180A/PABPC1 and model-90A/PABPC1 poly(A) RNPs by human PAN2-PAN3. Reactions were stopped and analyzed at the indicated time points on a 6% UREA-TBE PAGE and fluorescently imaged for Cy3 (RNA is labeled as outlined in A). The homemade Cy3-labeled RNA size marker is labeled with M.

(E) Densitometric quantitation of the deadenylation assays at each time point. The peak poly(A) lengths (in triplicate) are plotted against time. To illustrate differences in decay dynamics, quadratic polynomial models are fitted against the mean of the data and have an $R^2 > 0.9$ in both cases. The confidence interval is displayed in light gray.

See also Figure S1.

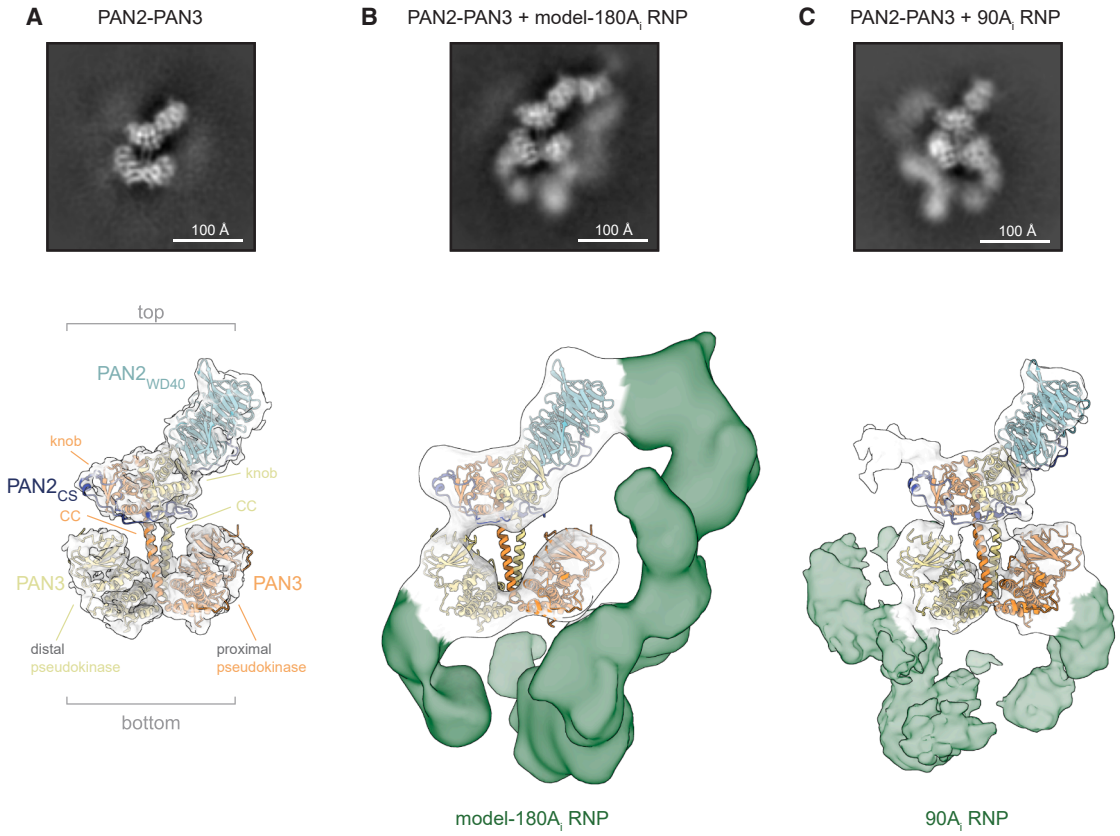

Figure 2. Structural basis underlying recognition of the poly(A) RNP by human PAN2-PAN3

The top images show the reference-free 2D class averages of apo human PAN2-PAN3 (A), human PAN2-PAN3 in the presence of the model-180A$_i$ RNP (B), and human PAN2-PAN3 in the presence of the 90A$_i$ RNP (C). 2D class averages are oriented to center the apo PAN2-PAN3. The white scale bar corresponds to 100 Å. The bottom images show the single-particle cryo-EM 3D reconstruction of apo human PAN2-PAN3 (A), human PAN2-PAN3 in the presence of the model-180A$_i$ RNP (B), and human PAN2-PAN3 in the presence of the 90A$_i$ RNP (C). The molecular model depicts the PAN3 dimer in yellow and orange, the PAN2 WD40 domain in cyan, and the PAN2 connecting segment (CS) in blue. The respective (model-)A$_i$ RNP density is depicted in green.
See also Figures S2 and S3 and Table S1.

length falls below the transition range preferred by PAN2-PAN3 and also allows a direct comparison with the yeast system (Figures 2C and S2). As a control, we reconstituted the corresponding yeast Pan2-Pan3-90A$_i$-Pab1 complex and examined it by cryo-EM. The 2D class averages showed a very similar structural organization to what we previously reported for the 90A RNP complex with a catalytically inactive Pan2-Pan3,[13] validating the approach of using an inhibitory RNP and active deadenylase for the human system (Figures S3A and S3B).[13,19] In the structure of the yeast complex, the 90A RNP is formed by the oligomerization of three Pab1 protomers and is recognized at multiple sites on the surface of the deadenylase: the 90A RNP contacts the WD40 domain of Pan2 with its most 5' portion, then extends diagonally over the two pseudokinase domains, and ultimately docks to the UCH-RNase module, pointing the RNA 3' end into the active-site pocket.[13] Although the single-particle cryo-EM analyses of the human RNP-containing complexes showed a preferred orientation more severe than what we observed for the yeast complex (Figure S2),[13] we could distinguish additional density features as compared to the apo state of the human deadenylase that could be attributed to the poly(A) RNPs (Figures 2 and S3).

In the structure of human PAN2-PAN3 with the model-180A$_i$ RNP, the density for the RNP complex contacts the PAN2 WD40 domain in a similar manner to the interaction observed for *S. cerevisiae* Pan2-Pan3.[13] From there, the RNP extends toward the proximal PAN3 pseudokinase, curving around this domain and contacting its bottom side. The central segment of the RNP density then continues in a sharp, prominent arch toward the bottom side of the distal pseudokinase (Figure 2B). The corresponding 2D class averages also revealed a halo of density near the distal PAN3 pseudokinase that likely corresponds to a partially flexible UCH-RNase module (Figures 2B and S3C).

In stark contrast to the budding yeast complex with a comparable poly(A) RNP, the structure of human PAN2-PAN3 with the shorter 90A$_i$ RNP revealed multiple binding states (Figure S3A). The reconstruction of the best-defined state (I) showed the RNP density only curving around the bottom sides of the two PAN3 pseudokinase domains but not interacting with the

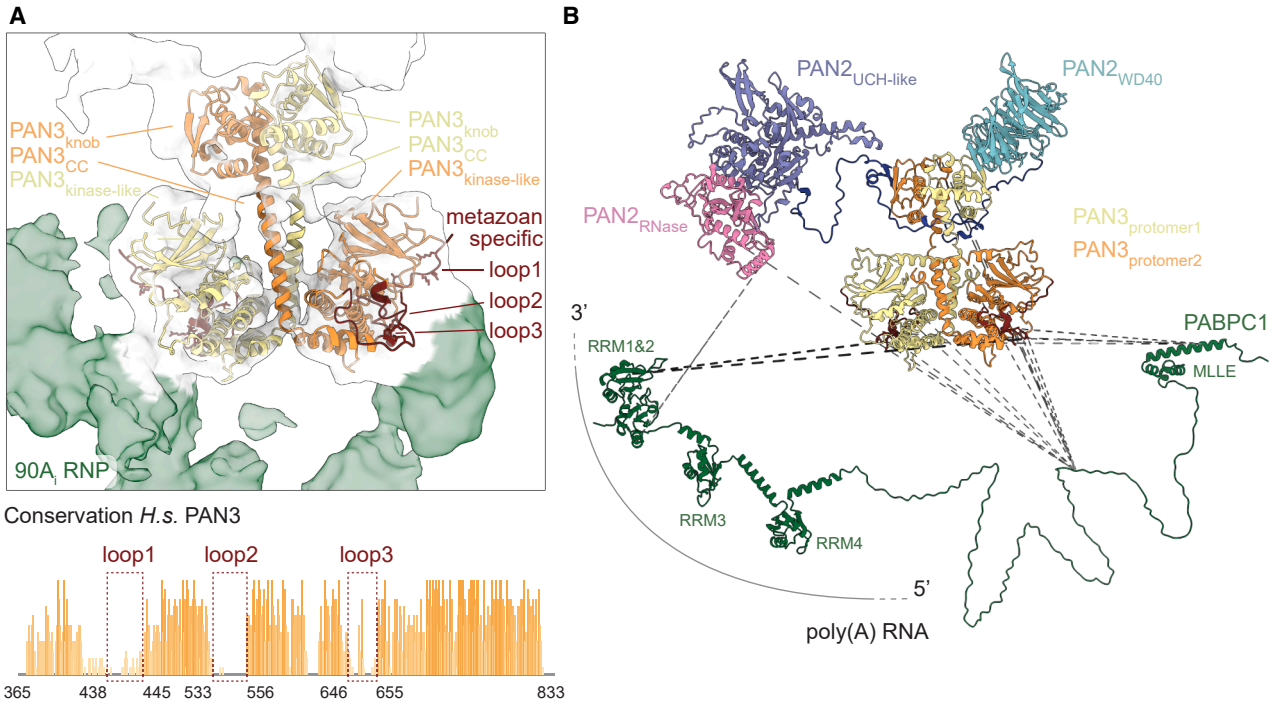

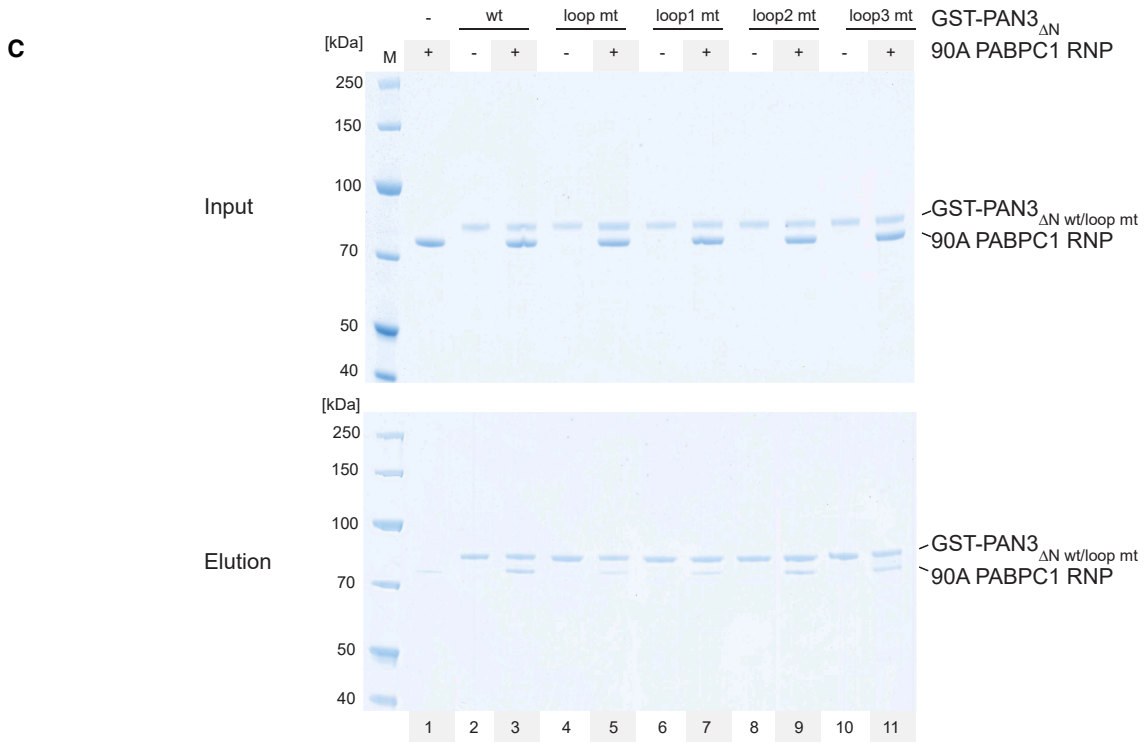

Figure 3. Metazoan-specific loops in the human PAN3 pseudokinase domains mediate interaction with the poly(A) RNP

(A) Molecular model of the human PAN3 dimer fitted into the single-particle cryo-EM reconstruction of PAN2-PAN3 in the presence of the 90A$_i$ RNP (as in Figure 2). The PAN3 metazoan-specific loops in the kinase domain are highlighted in red and labeled accordingly. The PAN3 dimer is colored in yellow and orange, and structural motifs are labeled accordingly. (Bottom) Bar plot of the PAN3 conservation shown in detail in Figure S4 and numbered according to human PAN3.

(legend continued on next page)

PAN2 WD40 domain (Figure 2C). We also observed the RNP density continuing after the distal pseudokinase domain, fading toward the expected position of the UCH-RNase module in the corresponding 2D class averages (Figure S3). Another set of 2D class averages (state Ib) showed an overall similar organization but with the RNP density instead fading in the opposite direction from the proximal pseudokinase toward the PAN2 WD40 domain (Figure S3B). We interpreted this as the RNP being bound with opposite directionality compared to state I. In yet another 2D class (state II), we observed the RNP arch only spanning between the PAN2 WD40 domain and the proximal pseudokinase, without detectable density reaching the distal pseudokinase (Figure S3B). Altogether, the different individual states observed with the 90A$_i$ RNP reflect portions of the single, continuous binding path observed for the longer 180A$_i$ RNP (Figure 2).

Thus, though the binding of the poly(A) RNP to the PAN2 WD40 domain is conserved from yeast to human[13] (Figure S3D), the overall poly(A) binding path on PAN3 has diverged between these species. While yeast Pan3 directs the poly(A) RNP along a short, diagonal path across the surface of the two pseudokinase domains, human PAN3 guides the central segment of the poly(A) RNP on a longer, curved trajectory around the two pseudokinase domains.

Poly(A) RNP recognition by human PAN2-PAN3

The structural analysis described above raised the question of what determines the specific poly(A) RNP binding path on human PAN3. When analyzing the poly(A)-RNP-interacting surfaces on the PAN3 homodimer, we noticed that the contact regions are located at apparently identical positions in the large lobes of the two pseudokinase domains (Figure 3A). These positions correspond to extended loop regions of PAN3 (loop1: 438–445, loop2: 533–556, and loop3: 646–655) that are conserved in metazoan sequences and absent in fungi (Figures 3A and S4A). Interestingly, these loops contain many positively charged and aromatic residues, typical of RNA/RNP interactions.[24]

We proceeded to validate these structural observations in biochemical experiments. First, we used crosslinking-mass spectrometry (XL-MS) analyses to support the interpretation of the protein-protein interactions. To limit the possibility of nonspecific crosslinking and increase the stringency of the experimental setup, we used a truncated form of PAN3 that lacks most of the N-terminal unstructured region (PAN3$_{\Delta N}$, residues 360–833) and analyzed the data, focusing on the crosslinks that were identified in all three technical replicates. The XL-MS analysis of recombinant human PAN2-PAN3$_{\Delta N}$ with a 90A RNP revealed interlinks between the RNase module of PAN2 and RNA-recognition motif 1 (RRM1)-RRM2 of PABPC1 (Figures 3B, S4B, and S4C). With this technique, we cannot distinguish which of the three PABPC1 protomers in the 90A RNP is engaged in a specific crosslinking contact. We note, however, that the RRM1-RRM2 module at the 3' end of the poly(A) RNA crosslinks with the deadenylase near the active site in the structure of the yeast complex,[13] supporting the interpretation that the poly(A) RNP is indeed engaged with the ribonuclease in the human complex. Furthermore, we observed multiple crosslinks between the PAN3 pseudokinase and PABPC1 (Figure S4C). In particular, the crosslink between Lys542 in loop2 of PAN3 and Lys78 in RRM1 of PABPC1 was also detected when subjecting only the PAN3$_{\Delta N}$ homodimer and a 90A RNP to a similar XL-MS analysis (Figure 3B).

Since the XL-MS approach identifies residues that are in close proximity rather than direct interactions, we investigated the contribution of the distinct PAN3 loop regions for poly(A) RNP binding. To this end, we performed pull-down experiments focusing on the PAN3 pseudokinase domain with recombinant GST-PAN3$_{\Delta N}$ as bait, assessing both the wild-type (WT) protein and mutants containing reverse-charge mutations in each loop (loop1 mt, loop2 mt, and loop3 mt) or combining all loop mutations (loop mt) (Figure 3C). The 90A RNP was used as prey in these assays, as the structural analyses suggested that it is sufficient to engage with both pseudokinase domains (Figure S3). The WT PAN3$_{\Delta N}$ homodimer indeed reproducibly co-precipitated the 90A RNP in these assays (Figure 3C, lane 3). In contrast, the PAN3$_{\Delta N}$ loop mt almost completely impaired binding (Figure 3C, lane 5). Interestingly, mutations in loop1 alone reduced binding to the 90A RNP almost as efficiently as the PAN3$_{\Delta N}$ construct with mutations in all three loops (Figure 3C lane 7). The mutants in loop2 and loop3 showed only a minor effect on the interaction (Figure 3C, lanes 9 and 11). Our structural and biochemical results thus reveal interactions between the poly(A) RNP and metazoan-specific loops of human PAN2-PAN3, with loop1 providing a direct contact and loop2 being in close proximity. These results point to a structural adaptation between the deadenylase complex and the extended poly(A) tails in metazoan mRNAs.[25]

DISCUSSION

In this study, we have uncovered the molecular basis by which the human PAN2-PAN3 deadenylase has adapted to recognize and trim the long poly(A) tails characteristic of human mRNAs (Figure 4; Video S1). To understand how human PAN2-PAN3 releases its grip on long poly(A) tails when they are shortened to 110–150 nt,[5,11] we obtained structural information with two poly(A) RNP substrates, one above and one below this transition range: a 180A RNP and a 90A RNP containing molar equivalents

(B) Intermolecular BS^3 crosslinks from triplicate XL-MS experiments between human PAN2-PAN3$_{\Delta N}$ and the 90A RNP (90A RNA and 3xPABPC1). PAN2-PAN3 is colored as in Figure 2, with the UCH-RNase module in violet and pink and PABPC1 in green. As a note, XL-MS cannot distinguish between different protomers, so only one PABPC1 protomer is mapped. The orientation of poly(A) RNA is indicated in the schematic in gray and labeled accordingly. The crosslinks are illustrated as dashed lines. The two black dashed lines highlight crosslinks between K542 in the metazoan PAN3-specific loop 2 and K78 in RRM1 of PABPC1, which also appeared in BS^3 crosslinking triplicates of the PAN3$_{\Delta N}$ homodimer vs. 90A RNP.
(C) Coomassie-stained 4%–12% SDS-PAGE showing pull-downs of 90A RNP by GST-tagged wild-type (WT) PAN3$_{\Delta N}$ or a GST-tagged PAN3$_{\Delta N}$ variant with charge-reversal mutations in all three metazoan-specific loops (loop mt) or in the individual loops (loop1 mt, loop2 mt, or loop3 mt). Mutated residues are depicted as sticks in (A). The top image shows the experimental input, and the bottom image shows the eluate from the GSH resin after extensive washes. M indicates the molecular weight marker.
See also Figure S4 and Data S1.

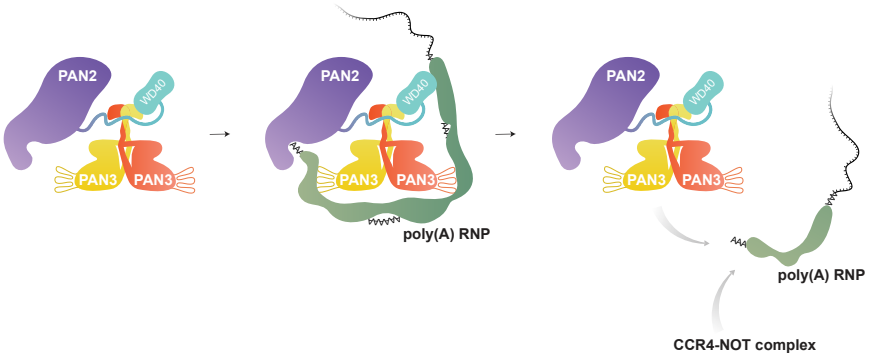

Figure 4. Long poly(A) RNPs are optimal substrates for human PAN2-PAN3

Mechanistic cartoon of the human PAN2-PAN3 interaction with poly(A) RNP. Human PAN2-PAN3 has multiple contact sites with long poly(A) RNPs (e.g., the 180A poly(A) RNP) by simultaneously binding to both the PAN2 WD40 domain and the UCH-RNase module, as well as the extended loop regions of the PAN3 kinase domains. The poly(A) tail is shortened and dissociates from PAN2-PAN3 and is eventually handed over to the CCR4-NOT deadenylase for further shortening.

See also Video S1.

of PABPC1 based on a 27-nt binding footprint.[26,27] By comparing our current findings with previous work on the corresponding system in budding yeast,[13] we have identified both conserved and divergent features that underlie a shared poly(A) trimming activity but different species-specific mechanisms of poly(A)-tail-length regulation.

The human PAN2-PAN3 deadenylase recognizes long poly(A) RNPs at distinct contact points (Figure 4). PAN2 recognizes the 5' and 3' ends of the poly(A) RNP at the WD40 domain and at the RNase active site, respectively. PAN3 binds the segment of the poly(A) RNP between them, serving as a scaffold that guides the substrate to curve around the two pseudokinase domains. The interactions of PAN2 with the ends of the poly(A) RNP are conserved from yeast to human,[13] except there is a more flexible connection of the ribonuclease module to the rest of the deadenylase complex (Figures 2 and S3). The contacts at the deadenylase WD40 domain appear to play a crucial role by contributing a major binding site as well as substrate directionality.[13] Notably, in the human context, this interaction at the WD40 domain occurs near a structural repeat that is absent in a disease-associated exon-skipping variant of PAN2[5] (PAN2 residues 192–217) (Figure S3D). In contrast to this, the interactions of PAN3 with the central segment of the mRNP have diverged from yeast to human. Interestingly, T/SW motifs of metazoan RNA-binding proteins (e.g., TRNC6) interact directly with the PAN3 pseudokinase domain at a site in close proximity to this central segment of the human poly(A) RNP.[23] Thus, even though PAN2-PAN3 and the poly(A)-binding protein PABPC1 are overall conserved from fungi to humans, specific differences embedded in the structure of the human deadenylase complex guide the recognition of a poly(A) RNP along a more extended surface, accommodating additional interactions with respect to the yeast orthologs.

By extrapolating from the known dimensions of poly(A) RNA recognition by the yeast poly(A)-binding protein Pab1,[13] we anticipate that a poly(A) stretch long enough to engage more than five PABPC1 molecules (i.e., longer than 150A) can fully cover the entire poly(A) RNP binding surface of human PAN2-PAN3. When the poly(A) RNP becomes further shortened, it loses its grip on the WD40 domain. While the transition is gradual, because of the flexibility of the PAN2 ribonuclease module, the definitive switch also likely occurs below 120A and four PABPC1. At this stage, the poly(A) RNP binds not only less efficiently but also probably less productively, with opposite directionalities. How the shortened poly(A) RNP is then recognized by CCR4-NOT, the deadenylase complex that leads to mRNA decay, is a quest for future studies.

Limitations of the study

One limitation is the resolution of the RNP-bound cryo-EM reconstructions, likely caused by the anisotropy of the data and low particle numbers. These problems are linked to the inherent difficulties of large poly(A) RNP reconstitutions.

Our model RNPs also lack additional parts of native mRNAs (5' UTR, coding sequence, and 3′ UTR) and possible associated proteins. The *in vivo* situation could therefore differ and is, in all likelihood, somewhat gene/transcript specific. However, the structures and activity assays with long poly(A) RNPs reported here serve as a proof of principle and pave the way for similar inquiries addressing these limitations in the future.

RESOURCE AVAILABILITY

Lead contact

Further information and requests for resources and reagents should be directed to and will be fulfilled by the lead contact, Elena Conti (conti@biochem.mpg.de).

Materials availability

The plasmids generated for this study will be made available upon request.

Data and code availability

- The cryo-EM density map has been deposited in the Electron Microscopy Data Bank (EMDB) and the Protein Data Bank (PDB), respectively, under the accession numbers EMDB: EMD-53362/PDB: 9QTU (human apo PAN2-PAN3), EMDB: EMD-53392 (human PAN2-PAN3 bound to 90Ai/PABPC1 RNP), and EMDB: EMD-53424 (human PAN2-PAN3 bound to 180Ai/PABPC1 RNP).
- Data of unprocessed and uncompressed imaging files are available at Mendeley Data: https://data.mendeley.com/preview/469k69dwp9?a=8a497ff2-2f1b-4f14-9ec9-2390c86d0663.
- This paper does not report original code.
- Any additional information required to reanalyze the data reported in this work/paper is available from the lead contact upon reasonable request.

ACKNOWLEDGMENTS

We are grateful to Tillman Schäfer and Daniel Bollschweiler at the MPIB Cryo-EM Facility (RRID: SCR_025744) for outstanding infrastructure and J. Rajan Prabu and Christian Benda for excellent maintenance of computational

infrastructure. We thank Barbara Steigenberger at the MPIB Mass Spectrometry Facility (RRID: SCR_025745) for mass spectrometry data acquisition. We thank Courtney Long for invaluable help in preparing the manuscript and Julia Kuhl for the drawing in Figures S3 and 4. We are grateful to Petra Birle, Tatjana Krywcun, Daniela Wartini, and Marc Baumgärtner for assistance. We greatly appreciate Nikolaus Rajewsky and Ivano Legnini, as well as all members of our group, for thoughtful discussions. E.C. acknowledges funding from the Max Planck Society, the European Research Council (Advanced Investigator Grant EXORICO [740329] and GOVERNA [101054447]), the German Research Foundation(SFB1035), and the Novo Nordisk Foundation ExoAdapt Grant (31199) and support from the NOMIS Foundation.

AUTHOR CONTRIBUTIONS

E.C. and I.B.S. conceptualized, initiated, and supervised the project; I.B.S. developed the protocols to produce mRNAs with long poly(A) tails; J.C.A., T.R., and I.B.S. performed all other experiments and analyzed the data; J.B. and S.S. developed the protein purification protocols; M.R. created the molecular animation; and J.C.A., T.R., I.B.S., and E.C. wrote the manuscript and prepared the figures.

DECLARATION OF INTERESTS

The authors declare no competing interests.

STAR★METHODS

Detailed methods are provided in the online version of this paper and include the following:

- KEY RESOURCES TABLE
- EXPERIMENTAL MODEL AND STUDY PARTICIPANT DETAILS
  - Origins of recombinant open reading frames
- METHOD DETAILS
  - Protein expression and purification
  - Poly(A) templates for *in vitro* RNA transcription
  - *In vitro* RNA transcription and fluorescent labeling
  - Pulldown assay with purified proteins
  - PAN2-PAN3 RNP crosslinking mass spectrometry
  - Deadenylation assays
  - Cryo-EM grid preparation and imaging
  - Cryo-EM data processing
  - Modeling and density fitting
  - Molecular animation
- QUANTIFICATION AND STATISTICAL ANALYSIS
  - Quantitation of *in vitro* deadenylation assays

SUPPLEMENTAL INFORMATION

Supplemental information can be found online at https://doi.org/10.1016/j.celrep.2025.116609.

Received: June 5, 2025
Revised: September 25, 2025
Accepted: November 4, 2025

REFERENCES

1. Passmore, L.A., and Coller, J. (2022). Roles of mRNA poly(A) tails in regulation of eukaryotic gene expression. Nat. Rev. Mol. Cell Biol. *23*, 93–106. https://doi.org/10.1038/s41580-021-00417-y.
2. Eckmann, C.R., Rammelt, C., and Wahle, E. (2011). Control of poly(A) tail length. Wiley Interdiscip. Rev. RNA *2*, 348–361. https://doi.org/10.1002/wrna.56.
3. Rodriguez-Molina, J.B., and Turtola, M. (2023). Birth of a poly(A) tail: mechanisms and control of mRNA polyadenylation. FEBS Open Bio *13*, 1140–1153. https://doi.org/10.1002/2211-5463.13528.
4. Eliseeva, I.A., Lyabin, D.N., and Ovchinnikov, L.P. (2013). Poly(A)-binding proteins: structure, domain organization, and activity regulation. Biochemistry. *78*, 1377–1391. https://doi.org/10.1134/S0006297913130014.
5. Yamashita, A., Chang, T.C., Yamashita, Y., Zhu, W., Zhong, Z., Chen, C.Y.A., and Shyu, A.B. (2005). Concerted action of poly(A) nucleases and decapping enzyme in mammalian mRNA turnover. Nat. Struct. Mol. Biol. *12*, 1054–1063. https://doi.org/10.1038/nsmb1016.
6. Zhao, Q., Pavanello, L., Bartlam, M., and Winkler, G.S. (2023). Structure and function of molecular machines involved in deadenylation-dependent 5'-3' mRNA degradation. Front. Genet. *14*, 1233842. https://doi.org/10.3389/fgene.2023.1233842.
7. Yi, H., Park, J., Ha, M., Lim, J., Chang, H., and Kim, V.N. (2018). PABP Cooperates with the CCR4-NOT Complex to Promote mRNA Deadenylation and Block Precocious Decay. Mol. Cell *70*, 1081–1088.e5. https://doi.org/10.1016/j.molcel.2018.05.009.
8. Beilharz, T.H., and Preiss, T. (2007). Widespread use of poly(A) tail length control to accentuate expression of the yeast transcriptome. RNA *13*, 982–997. https://doi.org/10.1261/rna.569407.
9. Brown, C.E., and Sachs, A.B. (1998). Poly(A) tail length control in Saccharomyces cerevisiae occurs by message-specific deadenylation. Mol. Cell Biol. *18*, 6548–6559. https://doi.org/10.1128/MCB.18.11.6548.
10. Mangus, D.A., Evans, M.C., Agrin, N.S., Smith, M., Gongidi, P., and Jacobson, A. (2004). Positive and negative regulation of poly(A) nuclease. Mol. Cell Biol. *24*, 5521–5533. https://doi.org/10.1128/MCB.24.12.5521-5533.2004.
11. Eisen, T.J., Eichhorn, S.W., Subtelny, A.O., Lin, K.S., McGeary, S.E., Gupta, S., and Bartel, D.P. (2020). The Dynamics of Cytoplasmic mRNA Metabolism. Mol. Cell *77*, 786–799.e10. https://doi.org/10.1016/j.molcel.2019.12.005.
12. Subtelny, A.O., Eichhorn, S.W., Chen, G.R., Sive, H., and Bartel, D.P. (2014). Poly(A)-tail profiling reveals an embryonic switch in translational control. Nature *508*, 66–71. https://doi.org/10.1038/nature13007.
13. Schafer, I.B., Yamashita, M., Schuller, J.M., Schussler, S., Reichelt, P., Strauss, M., and Conti, E. (2019). Molecular Basis for poly(A) RNP Architecture and Recognition by the Pan2-Pan3 Deadenylase. Cell *177*, 1619–1631.e21. https://doi.org/10.1016/j.cell.2019.04.013.
14. Reuter, M.S., Zech, M., Hempel, M., Altmüller, J., Heung, T., Pölsler, L., Santer, R., Thiele, H., Trost, B., Kubisch, C., et al. (2022). Biallelic PAN2 variants in individuals with a syndromic neurodevelopmental disorder and multiple congenital anomalies. Eur. J. Hum. Genet. *30*, 611–618. https://doi.org/10.1038/s41431-022-01077-y.
15. Maddirevula, S., AlZahrani, F., Anazi, S., Almureikhi, M., Ben-Omran, T., Abdel-Salam, G.M.H., Hashem, M., Ibrahim, N., Abdulwahab, F.M., Meriki, N., et al. (2018). GWAS signals revisited using human knockouts. Genet. Med. *20*, 64–68. https://doi.org/10.1038/gim.2017.78.
16. Scior, A., Preissler, S., Koch, M., and Deuerling, E. (2011). Directed PCR-free engineering of highly repetitive DNA sequences. BMC Biotechnol. *11*, 87. https://doi.org/10.1186/1472-6750-11-87.
17. Chen, C.Y.A., Zhang, Y., Xiang, Y., Han, L., Chang, J.T., and Shyu, A.B. (2017). Antagonistic actions of two human Pan3 isoforms on global mRNA turnover. RNA *23*, 1404–1418. https://doi.org/10.1261/rna.061556.117.
18. Baer, B.W., and Kornberg, R.D. (1980). Repeating structure of cytoplasmic poly(A)-ribonucleoprotein. Proc. Natl. Acad. Sci. USA *77*, 1890–1892. https://doi.org/10.1073/pnas.77.4.1890.
19. Tang, T.T.L., Stowell, J.A.W., Hill, C.H., and Passmore, L.A. (2019). Author Correction: The intrinsic structure of poly(A) RNA determines the specificity of Pan2 and Caf1 deadenylases. Nat. Struct. Mol. Biol. *26*, 988. https://doi.org/10.1038/s41594-019-0295-x.

20. Schafer, I.B., Rode, M., Bonneau, F., Schussler, S., and Conti, E. (2014). The structure of the Pan2-Pan3 core complex reveals cross-talk between deadenylase and pseudokinase. Nat. Struct. Mol. Biol. *21*, 591–598. https://doi.org/10.1038/nsmb.2834.

21. Wolf, J., Valkov, E., Allen, M.D., Meineke, B., Gordiyenko, Y., McLaughlin, S.H., Olsen, T.M., Robinson, C.V., Bycroft, M., Stewart, M., and Passmore, L.A. (2014). Structural basis for Pan3 binding to Pan2 and its function in mRNA recruitment and deadenylation. EMBO J. *33*, 1514–1526. https://doi.org/10.15252/embj.201488373.

22. Jonas, S., Christie, M., Peter, D., Bhandari, D., Loh, B., Huntzinger, E., Weichenrieder, O., and Izaurralde, E. (2014). An asymmetric PAN3 dimer recruits a single PAN2 exonuclease to mediate mRNA deadenylation and decay. Nat. Struct. Mol. Biol. *21*, 599–608. https://doi.org/10.1038/nsmb.2837.

23. Christie, M., Boland, A., Huntzinger, E., Weichenrieder, O., and Izaurralde, E. (2013). Structure of the PAN3 pseudokinase reveals the basis for interactions with the PAN2 deadenylase and the GW182 proteins. Mol. Cell *51*, 360–373. https://doi.org/10.1016/j.molcel.2013.07.011.

24. Corley, M., Burns, M.C., and Yeo, G.W. (2020). How RNA-Binding Proteins Interact with RNA: Molecules and Mechanisms. Mol. Cell *78*, 9–29. https://doi.org/10.1016/j.molcel.2020.03.011.

25. Kwon, A., Scott, S., Taujale, R., Yeung, W., Kochut, K.J., Eyers, P.A., and Kannan, N. (2019). Tracing the origin and evolution of pseudokinases across the tree of life. Sci. Signal. *12*, eaav3810. https://doi.org/10.1126/scisignal.aav3810.

26. Baer, B.W., and Kornberg, R.D. (1983). The protein responsible for the repeating structure of cytoplasmic poly(A)-ribonucleoprotein. J. Cell Biol. *96*, 717–721. https://doi.org/10.1083/jcb.96.3.717.

27. Sachs, A.B., Bond, M.W., and Kornberg, R.D. (1986). A single gene from yeast for both nuclear and cytoplasmic polyadenylate-binding proteins: domain structure and expression. Cell *45*, 827–835. https://doi.org/10.1016/0092-8674(86)90557-x.

28. Gat, Y., Schuller, J.M., Lingaraju, M., Weyher, E., Bonneau, F., Strauss, M., Murray, P.J., and Conti, E. (2019). InsP(6) binding to PIKK kinases revealed by the cryo-EM structure of an SMG1-SMG8-SMG9 complex. Nat. Struct. Mol. Biol. *26*, 1089–1093. https://doi.org/10.1038/s41594-019-0342-7.

29. Klykov, O., Steigenberger, B., Pektaş, S., Fasci, D., Heck, A.J.R., and Scheltema, R.A. (2018). Efficient and robust proteome-wide approaches for cross-linking mass spectrometry. Nat. Protoc. *13*, 2964–2990. https://doi.org/10.1038/s41596-018-0074-x.

30. Lagerwaard, I.M., Albanese, P., Jankevics, A., and Scheltema, R.A. (2022). Xlink Mapping and AnalySis (XMAS) - Smooth Integrative Modeling in ChimeraX. bioRxiv *2022.2004.2021*, 489026. https://doi.org/10.1101/2022.04.21.489026.

31. Schorb, M., Haberbosch, I., Hagen, W.J.H., Schwab, Y., and Mastronarde, D.N. (2019). Software tools for automated transmission electron microscopy. Nat. Methods *16*, 471–477. https://doi.org/10.1038/s41592-019-0396-9.

32. Zheng, S.Q., Palovcak, E., Armache, J.P., Verba, K.A., Cheng, Y., and Agard, D.A. (2017). MotionCor2: anisotropic correction of beam-induced motion for improved cryo-electron microscopy. Nat. Methods *14*, 331–332. https://doi.org/10.1038/nmeth.4193.

33. Biyani, N., Righetto, R.D., McLeod, R., Caujolle-Bert, D., Castano-Diez, D., Goldie, K.N., and Stahlberg, H. (2017). Focus: The interface between data collection and data processing in cryo-EM. J. Struct. Biol. *198*, 124–133. https://doi.org/10.1016/j.jsb.2017.03.007.

34. Punjani, A., Zhang, H., and Fleet, D.J. (2020). Non-uniform refinement: adaptive regularization improves single-particle cryo-EM reconstruction. Nat. Methods *17*, 1214–1221. https://doi.org/10.1038/s41592-020-00990-8.

35. Burt, A., Toader, B., Warshamanage, R., von Kügelgen, A., Pyle, E., Zivanov, J., Kimanius, D., Bharat, T.A.M., and Scheres, S.H.W. (2024). An image processing pipeline for electron cryo-tomography in RELION-5. FEBS Open Bio *14*, 1788–1804. https://doi.org/10.1002/2211-5463.13873.

36. Bepler, T., Morin, A., Rapp, M., Brasch, J., Shapiro, L., Noble, A.J., and Berger, B. (2019). Positive-unlabeled convolutional neural networks for particle picking in cryo-electron micrographs. Nat. Methods *16*, 1153–1160. https://doi.org/10.1038/s41592-019-0575-8.

37. Rosenthal, P.B., and Henderson, R. (2003). Optimal determination of particle orientation, absolute hand, and contrast loss in single-particle electron cryomicroscopy. J. Mol. Biol. *333*, 721–745. https://doi.org/10.1016/j.jmb.2003.07.013.

38. Abramson, J., Adler, J., Dunger, J., Evans, R., Green, T., Pritzel, A., Ronneberger, O., Willmore, L., Ballard, A.J., Bambrick, J., et al. (2024). Accurate structure prediction of biomolecular interactions with AlphaFold 3. Nature *630*, 493–500. https://doi.org/10.1038/s41586-024-07487-w.

39. Goddard, T.D., Huang, C.C., Meng, E.C., Pettersen, E.F., Couch, G.S., Morris, J.H., and Ferrin, T.E. (2018). UCSF ChimeraX: Meeting modern challenges in visualization and analysis. Protein Sci. *27*, 14–25. https://doi.org/10.1002/pro.3235.

40. Emsley, P., Lohkamp, B., Scott, W.G., and Cowtan, K. (2010). Features and development of Coot. Acta Crystallogr. D Biol. Crystallogr. *66*, 486–501. https://doi.org/10.1107/S0907444910007493.

41. Afonine, P.V., Poon, B.K., Read, R.J., Sobolev, O.V., Terwilliger, T.C., Urzhumtsev, A., and Adams, P.D. (2018). Real-space refinement in PHENIX for cryo-EM and crystallography. Acta Crystallogr. D Struct. Biol. *74*, 531–544. https://doi.org/10.1107/S2059798318006551.

STAR★METHODS

KEY RESOURCES TABLE

REAGENT or RESOURCE	SOURCE	IDENTIFIER
Bacterial and virus strains		
E. coli BL21 (DE3) STAR pRARE	Thermo Fisher Scientific	N/A
E. coli Omnimax	Thermo Fisher Scientific	N/A
Chemicals, peptides, and recombinant proteins		
H. sapiens PAN2 PAN3 and derivatives	This study and Schaefer et al., 2019	N/A
H. sapiens PABPC1	Schaefer et al., 2019	N/A
Phusion High-Fidelity PCR Master Mix	Thermo Fisher Scientific	F548
All used restriction enzymes	NEB	N/A
T7 polymerase	MPI of Biochemistry Core Facility	N/A
Spermidine	Sigma Aldrich	05292
ATP, CTP, GTP, UTP	Jena Bioscience	NU-1010 – 1013
Aminoallyl-UTP-X-Cy3	Jena Bioscience	NU-821-X-Cy3-L
RNase A (Biochemistry Grade)	Ambion	AM2274
T4-DNA-Ligase	NEB	N/A
DNase RNase free	Roche	04716728001
Wizard gel extraction kit	Promega	A9282
Quick Spin Columns G-50 Sephadex	Roche	11274015001
Proteinase K	NEB	P8107S
BS^3 (bis(Sulfosuccinimidyl)Suberat)	Thermo Scientific ™	A39266
Benzonase	MPI of Biochemistry Core Facility	N/A
Sf-900 II SFM medium	Thermo Fisher Scientific	10902104
FreeStyle 293 Expression Medium	Thermo Fisher Scientific	12338–018
Polyethylenimine	Polysciences, Inc.	23966
cOmplete™, EDTA-free protease inhibitor	Roche	5056489001
NuPAGE 4–12% Bis-Tris protein gels	Thermo Fisher Scientific	NP0321BOX
n-octyl-β-D-glucoside	Sigma-Aldrich	850511P
phenol:chloroform:isoamylalkohol (25:24:1)	Ambion	AM9730
chloroform:isoamylalkohol	SIGMA-ALDRICH	25668
Deposited data		
human PAN2-PAN3 deadenylase complex in the apo state	N/A	PDB: 9QTUEMDB: EMD-53362
human PAN2-PAN3 bound to a 90Ai/ PABPC1 RNP	N/A	EMDB: EMD-53392
human PAN2-PAN3 bound to a 180Ai/ PABPC1 RNP	N/A	EMDB: EMD-53424
Experimental models: Cell lines		
Human embryonic kidney 293T (HEK293T)	ATCC	CRL-3216
Trichoplusia ni Hi5 cells	Thermo Fisher Scientific	B85502
Spodoptera frugiperda Sf21 cells	Thermo Fisher Scientific	11497013
Oligonucleotides		
DNA oligonucleotides for construction of poly(A) library	ELLA Biotech	N/A
Synthetic 90A and 90Ai RNA	ELLA Biotech	N/A
Recombinant DNA		
pcDNA-3.1(+)	Thermo Fisher Scientific	V79020

(*Continued on next page*)

Continued

REAGENT or RESOURCE	SOURCE	IDENTIFIER
Software and algorithms		
Serial EM	Schorb et al., 2019	https://bio3d.colorado.edu/SerialEM/
Focus	Biyani et al., 2017	https://www.focus-em.org
MotionCor2	Zheng et al., 2017	https://msg.ucsf.edu/software/
CryoSPARC	Punjani et al., 2020	https://cryosparc.com
RELION-5.0	Burt et al., 2024	https://github.com/3dem/relion/tree/master
Topaz	Blepler et al., 2019	https://github.com/tbepler/topaz
AlphaFold3	Abramson et al., 2024	https://github.com/google-deepmind/alphafold3
ChimeraX	Goddard et al., 2018	https://www.cgl.ucsf.edu/chimerax/
Coot	Emsley et al., 2010	https://www2.mrc-lmb.cam.ac.uk/personal/pemsley/coot/
Phenix.refine	Afonine et al., 2018a	https://phenix-online.org/
Tidyverse	N/A	https://www.tidyverse.org/
Illustrator	Adobe	https//www.adobe.com
Other		
Quantifoil R2/1 Cu 200 mesh	Quantifoil	Q210CR1
StrepTactinXT	Cytiva	29401323
Superose^{TM} Increase 6 3.2/300	Cytiva	29091598
HiLoad 16/60 Superdex 200	Cytiva	28989335
HIS-SELECT® Nickel Affinity Gel	Sigma-Aldrich	H0537-25ML
GSH-resin	Pierce^{TM}Glutathione Magnetic Agarose	78601

EXPERIMENTAL MODEL AND STUDY PARTICIPANT DETAILS

Origins of recombinant open reading frames

Full length human PAN2, PAN3$_L$ and PABPC1 were cloned from the respective *H. sapiens* IMAGE clones (http://www.imageconsortium.org/) as described previously.[13] All PAN3 constructs used in this study are based on the 'short' splice variant of *H. sapiens* PAN3. This isoform was constructed by loop-out site directed mutagenesis to correspond to sequence Uniprot: Q58A45-3 (GenBank: XM_005266333/XP_005266390).[17]

The open reading frame of the PAN3 loop mutant (PAN3$_{\Delta N\ loop\ mt}$) was synthesised commercially and contains mutations of all arginine and lysines to serines, all asparagine to aspartic acid and all glutamine to glutamic acid in the three metazoan specific loops of PAN3 (N438D, R439S, Q441E, K442S, N445D, N533D, K540S, R541S, K542S, Q545E, N646D, Q652E, R653S, N655D). The individual loop mutants contain the following mutations: PAN3$_{\Delta N\ loop1\ mt}$ (N438D, R439S, Q441E, K442S, N445D); PAN3$_{\Delta N\ loop2\ mt}$ (N533D, K540S, R541S, K542S, Q545E) and PAN3$_{\Delta N\ loop3\ mt}$ (N646D, Q652E, R653S, N655D). The PAN2-PAN3$_{\Delta N}$ used for cross-linking assays in Figure 3B contains the ZTA-(Δ1-374)PAN3 construct. The GST-PAN3$_{\Delta N}$ used for pulldown assays has the domain boundaries of (Δ1-358)PAN3.

METHOD DETAILS

Protein expression and purification

Human PAN2-PAN3 variants (used for deadenylation assays and structural analysis) were expressed in HEK293 cells; human PAN2-PAN3$_{\Delta N}$ (PAN2 fl and 6xHis-ZTA-PAN3 Δ1-374 used for XL-MS) were expressed in Hi5 cells. Human PAN3 (6xHis-GST-PAN3 Δ1-358 used for pulldown assays) variants, as well as human PABPC1 (10xHis-PABPC1-StrepII) were expressed in *E. coli*. Protein expression in Hi5 insect cells and *E. coli* was carried out as described before.[13] The HEK 239T stable pools expressing PAN2-PAN3 in suspension were engineered and maintained as reported before in detail.[28]

HEK293 cell pellet of human PAN2-PAN3 was resuspended in lysis buffer containing 50 mM KH_2PO_4/K_2HPO_4 pH 8.0, 5 mM magnesium acetate, supplemented with 0.1% (v/v) NP-40, 4 mM dithiothreitol (DTT), 2 μg/mL DNase, 150 U/mL Benzonase, EDTA-free cOmplete Protease Inhibitor Cocktail (PIC) (Roche), 1 mM 4-(2-aminoethyl)benzenesulfonylfluoride hydrochloride (AEBSF), and 1/200 biolock (iba). The cleared lysate was subjected to a StreptactinXT column (Cytiva), washed with lysis buffer without NP-40 and subsequently with buffer containing 20 mM HEPES/NaOH pH 7.5, 400 mM NaCl, 0.1 mM $MgCl_2$, 0.1 mM $MnCl_2$, 4 mM DTT, and 1 mM AEBSF. The proteins were eluted in the latter buffer supplemented with 50 mM biotin. The elution was concentrated

and subjected to size exclusion chromatography (SEC) (HiLoad 16.60 Superdex 200 (Cytiva), equilibrated in 20 mM HEPES/NaOH pH 7.5, 400 mM NaCl, 0.1 mM $MgCl_2$,0.1 mM $MnCl_2$, and 4 mM DTT).

Insect cell pellet of human PAN2-PAN3$_{\Delta N}$ was resuspended in buffer containing 20 mM HEPES/NaOH, 400 mM NaCl, 0.1 mM $MgCl_2$, 0.1 mM $MnCl_2$, 5 mM β-mercaptoethanol (β-ME), supplemented with 2 μg/mL DNase, 150 U/mL Benzonase, PIC (Roche), 1 mM AEBSF and lysed by dounce-homogenizing. The cleared lysate was subjected to Ni-NTA resin (HIS-Select Nickel Affinity Gel) for 60 min at 4°C and subsequently washed extensively with lysis buffer. The proteins were eluted in lysis buffer supplemented with 300 mM imidazole, concentrated, and subjected to SEC (HiLoad 16/60Superdex200, equilibrated in 20 mM HEPES/NaOH pH 7.5, 400 mM NaCl, 0.1 mM $MgCl_2$, 0.1 mM $MnCl_2$ and 4 mM DTT).

E. coli expressed human PAN3$_{\Delta N\ wt/loop(x)\ mt}$ variants were purified as described for the insect cell expressed human PAN2-PAN3$_{\Delta N}$ with the difference being resuspension, washing, and eluting in buffer containing 50 mM KH_2PO_4/K_2HPO_4, 250 mM NaCl, 1 mM $MgCl_2$, 30 mM imidazole (500 mM imidazole for elution) and SEC equilibrated in buffer containing 20 mM HEPES/NaOH pH 7.5, 150 mM NaCl, 0.1 mM $MgCl_2$, 0.1 mM $MnCl_2$ and 4 mM DTT.

PABPC1-containing *E. coli* pellet was resuspended in lysis buffer containing 20 mM HEPES/NaOH, 400 mM NaCl, 8 mM β-ME, PIC (Roche), 1 mM AEBSF, 4 μg/mL DNase, and 150 U/mL Benzonase. Following sonication and centrifugation, the cleared lysate was mixed with Ni-NTA resin (HIS-Select Nickel Affinity Gel) and incubated for 60 min at 4°C. After washing with lysis buffer (without Benzonase and DNase) the protein was eluted in lysis buffer supplemented with 400 mM Imidazole. The elution was dialyzed overnight in 20 mM HEPES/NaOH pH 7.5, 50 mM KCl, 4 mM DTT, 10% (v/v) glycerol, and recombinant TEV protease for tag cleavage. PABPC1 was further purified via a Heparin column (Cytiva) (linear gradient from dialysis buffer to 50% buffer containing 20 mM HEPES/NaOH pH 7.5, 1000 mM KCl, 4 mM DTT) and polished on SEC (HiLoad 16/60 Superdex 200, equilibrated in 20 mM Tris/HCl pH 7.4, 500 mM NaCl, 0.1 mM $MgCl_2$ and 4 mM DTT).

Poly(A) templates for *in vitro* RNA transcription

To generate DNA templates for the *in vitro* RNA transcription of the model substrates with defined poly(A) tail lengths, we used an approach similar to what has been described previously for RNA substrates with short poly(A) tails.[16] In brief, we cloned annealed DNA oligos with poly(A) stretches of defined lengths (30A or 60A) into the HindIII and XhoI restriction sites of the pcDNA 3.1(+) vector. These annealed DNA oligos carried, upstream of the XhoI site, a BsmBI site (a Type IIS restriction enzyme), which cleaves five adenosines into the poly(A) stretch and leaves a sticky end with an overhang of four bases. To extend the poly(A) stretch further, we digested positive clones with BsmBI and XhoI followed by T4-DNA ligase mediated ligation of a dsDNA oligo carrying a matching overhang to the BsmBI cleavage site at the 5′ and again a BsmBI site followed by a XhoI site at the 3'. This design allowed for multiple successive rounds of digestion, ligation and plasmid preparation and extended the poly(A) stretch to a maximum of 240A in 30A steps (exception is the model-70A in which we extended from the model-60A using a 10A oligo of the same design). Positive clones were confirmed by analytical restriction digest, Sanger sequencing and preliminary *in vitro* RNA transcription. For the model-180A$_i$ (model-175A-GGG-AA), we used the model-150A and extended it with a 25A-GGG-AA stretch. Our model-poly(A) naming convention of the plasmids and the above-mentioned length explanations refer to the RNA level. All model-poly(A) constructs have on the DNA level one additional adenosine at the 3′ end of the poly(A) stretch to account for BsmBI mediated cleavage for *in vitro* transcription template generation.

A critical point while developing protocols to construct and propagate these plasmids was optimisation of culturing conditions of the carrier *E. coli* Omnimax strains. This effect is relevant for all RNA substrates studied here with poly(A) tails longer than the model-120A in our hands. Using the standard 37°C as cultivation temperature resulted in truncated model-poly(A) constructs most likely caused by recombination events in the homotypical adenosine stretches of the plasmids. This effect was limited when reducing all growth temperatures to room temperature (22°C), which allowed transformation and clonal propagation of the *E. coli* cultures carrying the respective plasmids. To additionally limit this truncation effect in *E. coli* transformations, we used a modified on-plate heat shock protocol with the LB agar plates pre-warmed to 22°C instead of 37°C.[13]

In vitro RNA transcription and fluorescent labeling

To generate templates for the T7 RNA polymerase-mediated *in vitro* RNA transcription with co-transcriptional Cy3 labeling, we digested the pcDNA 3.1-based model-poly(A) plasmids with NdeI and BsmBI. The fragments containing the MCS and the poly(A) tails were isolated using TBE-agarose gel electrophoresis. The T7-polymerase reaction was carried out for 4h at 37°C in the following transcription buffer: 40 mM Tris/HCl pH 8.0, 28 mM $MgCl_2$, 0.01% (v/v) Triton X-100, 5 mM DTT, 1 mM Spermidine. The cleanest transcription results with Cy3 labeling were achieved with a nucleotide mix at final concentrations of 10 mM ATP, 10 mM CTP, 10 mM GTP, 0.5 mM UTP supplemented with 0.25 mM Aminoallyl-UTP-X-Cy3. The DNA template was removed from the reaction by DNaseI digest and the resulting products (35nt+poly(A) tail of variable length) purified using phenol/chloroform extraction followed by ethanol precipitation. For the model-180A$_i$, RNA transcription was carried out similarly while using nucleotide concentrations of 10 mM ATP, 10 mM CTP, 10 mM GTP and 10 mM UTP.

Pulldown assay with purified proteins

For the pulldown assay described in Figure 3C, PABPC1 at a final concentration of 12.5 μM was incubated with a commercial 90A RNA oligo at a final concentration of 3 μM in RNP-reconstitution buffer (20 mM HEPES/NaOH pH 7.5, 400 mM NaCl, 0.1 mM $MgCl_2$,

0.1 mM $MnCl_2$, 4% glycerol (v/v), 4 mM DTT, 0.01% (v/v) NP-40) for 30 min on ice. Following RNP formation, NaCl concentration was adjusted to 50 mM by dilution, and N-terminally GST-tagged $PAN3_{\Delta N\ wt/loop(x)\ mt}$ homodimer was added to a final concentration of 3 μM and incubated for an additional 30 min on ice.

Samples were exposed to GSH resin (Pierce Glutathione Magnetic Agarose) for 1 h at 4°C under agitation. Unbound proteins were removed by three successive washes with 0.5 mL of pulldown buffer (20 mM HEPES/NaOH pH 7.5, 50 mM NaCl, 0.1 mM $MgCl_2$, 0.1 mM $MnCl_2$, 4% (v/v) glycerol, 4 mM DTT, 0.01% (v/v) NP-40). Bound proteins were eluted using elution buffer (pulldown buffer 'emented with 50 mM reduced glutathione).

Eluted samples were mixed with SDS-loading buffer, separated by SDS-PAGE on 4–12% NuPAGE gradient gels (Thermo Fisher Scientific), and visualized by Coomassie staining.

PAN2-PAN3 RNP crosslinking mass spectrometry

For intermolecular BS^3 crosslinking described in Figure 3B, the mRNP was reconstituted as described for the pulldown assay. Following RNP formation, NaCl concentration was adjusted to 50 mM by dilution and either PAN2-$PAN3_{\Delta N}$ or $PAN3_{\Delta N}$ homodimer was added to a final concentration of 3 μM and incubated for another 30 min on ice to allow complex formation. Crosslinking was initiated by adding bis(Sulfosuccinimidyl)Suberat (BS^3, Thermo Fisher Scientific) to a final concentration of 500 μM, followed by incubation at room temperature for 20 min. The crosslinking reaction was quenched by adding Tris/HCl (pH 7.5) to a final concentration of 8.25 μM.

Cross-linked proteins were denatured by the addition of 4 M urea in 50 mM Tris buffer (pH 8.0). For reduction and alkylation, 40 mM 2-chloroacetamide (CAA, Sigma-Aldrich) and 10 mM tris(2-carboxyethyl)phosphine (TCEP, Thermo Fisher Scientific) were introduced. After incubating for 20 min at 37°C, the samples were diluted 1:3 with MS-grade water (VWR). Proteins were then digested overnight at 37°C by the addition of 1 μg of LysC and 2 μg of trypsin (Promega). Following digestion, the solution was acidified with trifluoroacetic acid (TFA, Merck) to a final concentration of 1%, and peptides were desalted using Sep-Pak C18 1cc vacuum cartridges (Waters). Peptides (200 ng) were loaded onto Evotips Pure (Evosep).

The Evotips were eluted onto a 15-cm column (PepSep C18, 15 cm × 15 cm, 1.5 μm, Bruker Daltonics) using the Evosep One HPLC system and separated using the 30 SPD method. The mass spectrometer Orbitrap Exploris 480 (Thermo Fisher) was operated in data-dependent mode, with survey scans from m/z 300 to 1650 Th (resolution of 60k at m/z = 200 Th). Up to 15 of the most abundant precursors were selected and fragmented using stepped higher-energy C-trap dissociation (HCD) with normalized collision energies of 19, 27 and 35. MS2 spectra were recorded with a dynamic m/z range (resolution of 30k at m/z = 200 Th). Normalized AGC targets for MS1 and MS2 scans were set to 300% and 100%, respectively, with a maximum injection time of 25 ms for the MS1 scan. The maximum injection time for MS2 scans was set to 'auto'. Charge state 2 was excluded from fragmentation to enrich the fragmentation scans for cross-linked peptide precursors.

The acquired raw data were processed using Proteome Discoverer (version 2.5.0.400) with the integrated XlinkX/PD nodes.[29] To identify crosslinked peptide pairs, a database search was performed against a FASTA file containing the sequences of the proteins under investigation. BS3 was set as the crosslinker. Cysteine carbamidomethylation was specified as a fixed modification, while methionine oxidation and protein N-terminal acetylation were set as dynamic modifications. Trypsin/P was selected as the protease, with up to two missed cleavages allowed. Identifications were only accepted with a minimum score of 40 and a minimum delta score of 4. A 1% false discovery rate (FDR) at the peptide level was applied for filtering. Crosslinks were visualized in USCF ChimeraX using the XMAS extension.[30]

Deadenylation assays

Deadenylation reactions were carried out at 30°C for 60 min in a total reaction volume of 40 μL with 200 nM of poly(A) RNP and 100 nM of PAN2-PAN3 in a buffer containing 20 mM HEPES/NaOH, pH 7.5, 100 mM NaCl, 0.1 mM $MgCl_2$, 0.1 mM $MnCl_2$, and 4 mM DTT. The poly(A) RNP was reconstituted by mixing the respective Cy3-labeled model substrate RNAs at a final concentration of 2 μM (10×) with PABPC1 at a final concentration of 18 μM (1.5 × final RNA concentration x theoretical number of PABPC1 binding sites on substrate) in case of the reactions with the 180A-model substrate and 9 μM in case of the reactions with the 90A-model substrate. This mixture was incubated for 30 min at 4°C in a buffer containing 50 mM HEPES/NaOH pH 7.5 and 400 mM NaCl. The reaction started by the addition of the PAN2-PAN3 complex. At the indicated time points, 5 μL of each sample were removed and the deadenylation reaction was immediately stopped by the addition of 1.3 μL 5× stop buffer composed of 50 mM EDTA and 0.1% (v/v) SDS. Proteins were removed by Proteinase K (NEB) digest and diluted with 6.6 μL loading dye containing 10 mM EDTA, 0.1% (w/v) Orange G and 0.1% in formamide and boiled at 95°C for 4 min. The products were resolved on a 6% TBE (Tris-borate-EDTA)-polyacrylamide gel containing 7 M Urea. For molecular weight markers, we used mixed Cy3-labeled model RNAs with poly(A) tails of indicated length. Gels were imaged with a Typhoon FLA9500 at 532 nm (Cy3) and analyzed densitometrically in R using the tidyverse collection of R packages.

Cryo-EM grid preparation and imaging

The PAN2-PAN3–$90A_i$ RNP was reconstituted by mixing the individual components and incubating on ice for 5 min. Fresh peak fractions of PAN2-PAN3 of a Superose 6 3.2/300 (Cytiva) size exclusion were used at a final concentration of 380 nM. The $90A_i$ RNP was reconstituted via gel filtration over a Superdex 200 increase 3.2/300 column (Cytiva) and used at a final AU_{280nm} of 0.2 (typical

OD_{260nm}/OD_{280nm} of >2 were indicative of RNA presence). Both SEC runs were carried out in the above-mentioned gel filtration chromatography buffer. For the reconstitution of the PAN2-PAN3 model-180A_i RNP a similar protocol was followed. The peak fraction of a fresh gel-filtered PAN2-PAN3 preparation was used at a final concentration of 400 nM which was mixed with the peak fraction of a model-180A_i RNP reconstitution of a size exclusion column at a final AU_{280nm} of 0.24 (typical OD_{260nm}/OD_{280nm} of >2 were indicative of RNA presence). For grid preparation, n-octyl-β-D-glucoside was added to a final concentration of 0.04% (v/v) and 4 μL of this sample was applied to glow discharged (2.2×10^{-1} mbar for 2 × 20sec) Quantifoil holey carbon grids (R2/1, 200 mesh, Quantifoil). The grids were plunge vitrified into a liquid ethane/propane mix using a Vitrobot Mark IV at 4°C and 95% humidity. Cryo-EM data were collected on a FEI Titan Krios microscope operated at 300 kV, equipped with a post-column GIF (set to a slit width of 20 e^-) and a K3 direct detector operating in counting mode.

In the case of the PAN2-PAN3 90A_i RNP sample a total of 23 779 movies were recorded at a nominal magnification corresponding to 0.8512 Å/pixel at the specimen level. Initial screening data indicated severe preferred orientation with only one dominant view apparent in 2D and 3D processing trials (data not shown here). Since no other approach tested overcame this problem, we implemented a similar approach to before whereby we collected the data in 3 groups using a Multihole-Multishot stage tilt strategy in SerialEM: with 0° (4 316 micrographs; 5 × 5 hole matrix and 4 images per hole), with 15° (5 083 micrographs; 5 × 3 hole matrix and 4 images per hole) and with 30° (14 380 micrographs; 5 × 1 hole matrix and 4 images per hole).[13,31] In all groups, we imaged with a total exposure of 70 $e^-/Å^2$ at the specimen level evenly distributed over 35 frames during 3.5 s. As a preset target global defocus range, we used 0.5 to 2.8 μm. The PAN2-PAN3 model-180A_i RNP data were collected at a nominal magnification corresponding to 0.8512 Å/pixel at the specimen level with a total exposure of 69 $e^-/Å^2$ at the specimen level evenly distributed over 30 frames during 3 s using a Multihole-Multishot scheme with a 5 × 5 hole matrix and 7 images per hole.[31] No stage pretilt was employed. The target defocus ranged between 0.8 and 2.4 μm.

Cryo-EM data processing

For both reported datasets, the PAN2-PAN3 90A_i RNP and the PAN2-PAN3 model-180A_i RNP data, the correction of beam induced motion and dose-weighting was performed in MotionCor2 operated through the Focus software suit.[32,33] Focus was also employed to automatically discard micrographs based on too high contrast (e.g., crystalline surface ice) or movement beyond the correction capabilities of MotionCor2. If not stated otherwise, all further processing was carried out in CryoSPARC or RELION-5.0.[34,35] CTF parameters were determined using patch_ctf in CryoSPARC to account for the defocus gradient across micrographs in the pretilted data. For reasons of consistency the PAN2-PAN3 model-180A_i RNP data were also processed similarly. Particles were initially picked in both datasets using the template picker in CryoSPARC with low-pass filtered 2D class averages of earlier screening datasets as templates. Using particles belonging to 2D classes that clearly indicated the presence of PAN2-PAN3 and the poly(A) RNP a Topaz particle picking model was trained and used to pick and extract particles from micrographs of both datasets.[36] After several rounds of 2D classification to eliminate contamination, we calculated three initial 3D models for the PAN2-PAN3 90A_i RNP data, and further used these as starting models in one round of heterologous 3D refinement. The reconstruction with the lowest noise and highest degree of map connectivity was chosen for further 3D refinement. We obtained the most convincing reconstruction using the non-uniform 3D refinement routine in CryoSPARC. We also used the non-RNP bound particle stack from these data, consisting of 34 171 particles, to calculate a 3D reconstruction of the apo PAN2-PAN3 with no poly(A) RNP bound. For the PAN2-PAN3 model-180A_i RNP data, we only calculated two initial models which were subsequently used in heterogeneous 3D refinement followed by homogeneous 3D refinement and *ad hoc* low pass filtering to 20 Å in RELION. We are considering all resolution estimates quoted here as overestimates (in the PAN2-PAN3 model-180A_i RNP case as a drastic overestimate) in all likelihood caused by the severe anisotropy of the data and the low number of particles in the RNP-bound reconstructions. We still quote these estimates as useful proxies for the overall relative level of detail, connectivity and signal-to-noise ratio of these reconstructions, fully acknowledging the differences in local resolution from higher in the PAN2-PAN3 core but lower in the poly(A) RNP. In Figure S2E, we plotted the FSC of the independent half-maps after mask auto tightening ('tight') from the respective 3D refinement, while in the EMDB we deposited the corrected FSCs after noise substitution. For the PAN2-PAN3 model-180A_i RNP there is a discrepancy in the automatically determined resolution according to the 0.143 cut off criterion for the FSC of the independent half-maps (14 Å in RELION, 10 Å in CryoSPARC).[37]

Modeling and density fitting

In the 3D reconstruction of the human apo PAN2-PAN3 we were not able to observe any clear ordered density for neither the N-terminal part of PAN3 nor the UCH-RNase module of PAN2. In a first model building step we therefore used AlphaFold3.[38] AF3Complex predicts direct physical interactions in multimeric proteins with deep learning to predict models of the dimeric human PAN3 without most of the flexible N terminus, Δ(1–375)PAN3, in complex with human PAN2 without the UCH-RNase module, PAN2Δ(465–1202). After positioning this PAN2-PAN3 model into the apo PAN2-PAN3 reconstruction, individual parts were rebuilt. In brief, we removed residues 1–60 from PAN2 and the N-termini of the PAN3 protomers up to residue 416 due to lack of clear density for these parts.

The resulting final model and the cryo-EM map of the full PAN2-PAN3 RNP are in good agreement as determined by the correlation coefficients of as well as the FSC between both (see Table S1).

For all reconstructions rigid body fits were performed in USCF ChimeraX.[39] The model was manually adjusted in Coot and real space refined in phenix.refine.[40,41] Progress in modeling was monitored via the map-to-model correlation coefficients and map vs. model FSCs (see Table S1). Structure figures were created in ChimeraX.[39]

Molecular animation

The 3D molecular animation is primarily based on the structural data generated in this study and in[13] (PDB:9QTU and PDB:6R5K). The additional IDRs shown at the beginning of the movie were modeled based on Alphafold predictions.[38] The molecular models were converted into polygonal meshes using ChimeraX[39] and imported into Autodesk Maya. They were then animated using keyframe interpolation to and from the reference structure (shown in the movie at timepoint 00:16), to reflect the current hypothesis of how the molecular mechanism might proceed dynamically. The animation was rendered as a series of images and final compositing was done using Adobe After Effects.

QUANTIFICATION AND STATISTICAL ANALYSIS

Quantitation of *in vitro* deadenylation assays

The quantitation shown in Figures 1E and S1E was performed in R using the tidyverse collection of R packages as described before in detail.[13] In brief, densitometry was performed on Cy3-fluorescent scans of the UREA-PAGE gels of triplicate deadenylation time-course experiments. These data were calibrated for poly(A) tail length using the homemade Cy3 labeled model-poly(A) markers. Peak poly(A) tail lengths per time point were identified and plotted against deadenylation time. To qualitatively illustrate the different dynamics of the model-90A in contrast to the model-180A deadenylation time courses we fitted second order polynomial models against the mean of those data. We estimated initial decay rates of the model-90A and model-180A by fitting log-linear models against the normalised peak area data per time point for a 10A interval around the theoretical lengths of the substrate (model-180A vs. model-90A).